The dependence of transient climate sensitivity and radiative feedbacks on the spatial pattern of ocean heat uptake

Brian E. J. Rose,[1] Kyle C. Armour,[2] David S. Battisti,[3] Nicole Feldl[4] and Daniel D. B. Koll[5]

[1]Department of Atmospheric and Environmental Sciences, University at Albany

[2]Earth, Atmospheric and Planetary Sciences, MIT

[3]Atmospheric Sciences, University of Washington

[4]Geological and Planetary Sciences, Caltech

[5]Geophysical Sciences, University of Chicago

The effect of ocean heat uptake (OHU) on transient global warming is studied in a multi-model framework. Simple heat sinks are prescribed in shallow aquaplanet ocean mixed layers underlying atmospheric general circulation models, independently and combined with CO_2 forcing. Heat sinks are localized to either the tropics or high latitudes, representing two distinct modes of OHU found in coupled simulations. Tropical OHU produces modest cooling at all latitudes, offsetting only a small portion of CO_2 warming. High-latitude OHU produces strongly polar-amplified cooling that is three times more effective at offsetting CO_2. Each forcing generates distinctly different local and global radiative feedbacks, while differences in atmospheric energy transport set the pattern of temperature change. Thus transient global and regional warming depend sensitively on regional ocean processes determining the (evolving) spatial pattern of OHU.

1. Introduction

Ocean heat uptake (OHU) has long been recognized as critical in setting the pace of climate change [*Hansen et al.*, 1985; *Raper et al.*, 2002]. The deep oceans are warmed through a variety of vertical heat transport processes [*Gregory*, 2000] that delay warming at the surface. Ocean temperature trends over recent decades indicate 0.5-1 W m^{-2} global-mean OHU [*Hansen et al.*, 2005; *Lyman et al.*, 2010; *Balmaseda et al.*, 2013]. The Earth is in radiative disequilibrium—and cooler than it would otherwise be—due to OHU offsetting a substantial portion of the roughly 2 W m^{-2} present radiative forcing. Such is the traditional view of the role of OHU in transient climate sensitivity.

However, observations [*Yu and Weller*, 2007] and coupled general circulation model (GCM) simulations [*Winton et al.*, 2010; *Bitz et al.*, 2012] suggest that the geographic pattern of OHU is far from uniform or steady (see auxiliary material). A key question, then, is whether the global-mean surface warming is sensitive to the pattern of OHU. *Winton et al.* [2010] introduce an "efficacy" parameter in the global-mean energy budget to account for the inter-model spread in sensitivity of global surface temperature to OHU relative to radiative forcing, and find the largest efficacy when OHU occurs preferentially at high latitudes [see also *Bitz et al.*, 2012]. *Armour et al.* [2013] offer an explanation in terms of the spatial pattern of atmospheric radiative feedback (the local linearized relationship between top-of-atmosphere (TOA) radiative response and surface warming). To the extent that suppression of surface warming by OHU is primarily local, we expect OHU to affect global-mean temperature most strongly when co-located with regions of net positive (destabilizing) local feedback, typically also found at high latitudes [*Armour*

et al., 2013]. However it is not clear that the far-field temperature effects of OHU should be negligible, nor that local radiative feedbacks should remain constant in time as assumed by *Armour et al.* [2013]. An evolving OHU pattern may influence atmospheric structure sufficiently to modify local feedbacks.

Here we study the direct connection between the spatial pattern of OHU, radiative feedback, and temperature response. We analyze a series of idealized mixed-layer aquaplanet model simulations, wherein we prescribe OHU through a 'q-flux' that removes heat from the ocean mixed layer with a particular geographic pattern—mimicking the deep ocean's role in the coupled climate system. We compare two distinct OHU patterns, one centered at sub-polar latitudes ($\equiv q_{upH}$) and the other localized within the tropics ($\equiv q_{upT}$), that each produce the same area-weighted global-mean OHU ($\equiv A_{up}$, which we set to 2 W m^{-2}, roughly half the radiative forcing from a doubling of CO_2). The patterns are steady in time, symmetric about the equator and zonally, and varying in latitude ϕ by

$$q_{upH} = \min\left(0, -\frac{299 A_{up}}{90\cos(\frac{2\pi}{9})}\sin\left(\frac{18}{5}(|\phi| - \frac{2\pi}{9})\right)\right) \quad (1)$$

$$q_{upT} = \min\left(0, -\frac{16 A_{up}}{3\sqrt{3}}\cos(3\phi)\right), \quad (2)$$

q_{upH} peaks around 9 W m^{-2} at 65° latitude and is zero at the poles and equatorward of 40°, while q_{upT} peaks around 6 W m^{-2} at the equator and is zero poleward of 30° (Fig.1b-c). These OHU patterns broadly capture those found within coupled GCMs under transient warming (see auxiliary material).

We address two sets of questions. First, how does the spatial pattern of OHU affect the surface temperature response (both global mean and spatial pattern)? And second, can these differences be understood in terms of fixed underlying local radiative feedbacks, or

are the feedbacks themselves sensitive to the OHU pattern? We prescribe q_{upT} and q_{upH} independently and in conjunction with a doubling of CO_2. These simulations are thus a direct test of the degree to which OHU can compensate for an imposed radiative forcing, depending on its geographic structure. We propose that they serve as a challenge to the traditional, global-mean view of OHU, and as a guide to understanding the complex role of oceans in regional and global climate change.

2. Model inter-comparison

In order to assess robustness of our results, we use four different GCMs (Table 1), all configured as idealized slab ocean aquaplanets. CAM3 [*Collins et al.*, 2004] is the atmospheric component of NCAR's CCSM3 model; CAM4 uses a newer dynamical core and updated deep convection and cloud fraction schemes [*Neale et al.*, 2013]; AM2.1 is the atmospheric component of GFDL's CM2.1 model [*Delworth et al.*, 2006]. MITgcm is a 5-level model with simplified moist physical parameterizations [*Molteni*, 2003; *Rose and Ferreira*, 2013]. This model's crude 4-band radiative scheme precludes carrying out a $2\times CO_2$ experiment.

Our aquaplanet setup follows *Lee et al.* [2008], and is similar to the "aqua-planet experiment" of *Neale and Hoskins* [2001], except that we use energetically consistent mixed-layer ocean models with prognostic sea-surface temperature (SST). Perpetual equinox insolation is prescribed with solar constant 1365 W m^{-2}. Mixed layer depth is 10 m. Sea-surface albedo is fixed at 0.1. Control simulations are performed with 348 ppmv CO_2, 1650 ppbv CH_4 and 306 ppbv N_2O (all other greenhouse gases set to zero). Ozone has a prescribed steady, symmetric distribution [*Blackburn and Hoskins*, 2013]. Sea ice is omitted but

SST below freezing is permitted. Each simulation (control and forced) is integrated to equilibrium, at least 10 years.

The climatic impacts of CO_2 and OHU are shown in Fig.1 as time- and zonal-mean SST anomalies relative to each model's control simulation. The control climates differ between models, but feature warm equatorial SSTs around 30°C and cold polar SSTs near -40°C. The large equator-to-pole SST gradient is a consequence of equinoctial insolation.

Fig.1a shows warming from $2\times CO_2$ as well as the combined effects of $2\times CO_2$ and OHU (analogous to transient climate sensitivity). CO_2 alone produces the familiar polar-amplified warming pattern (solid lines). Equilibrium sensitivity to $2\times CO_2$ is about 1.8 K (Table 1). The very small inter-model spread suggests we might be under-sampling the uncertainty in climate feedback. The deliberate elimination of surface ice and snow from our simulations likely contributes to this.

Fig.1a also shows that OHU mitigates the CO_2 warming, as expected. However this effect is very sensitive to the location of OHU. For high-latitude OHU (q_{upH}), only 2 W m^{-2} of global OHU is necessary to fully cancel 4 W m^{-2} of greenhouse gas warming (Table 1, dashed curves in Fig.1a). The same OHU limited to the tropics (q_{upT}, dotted curves) mitigates global warming by only a third (about 0.6°C, Table 1). The cooling due to OHU alone (Fig.1b-c) is similarly dependent on spatial pattern of the uptake. In the global mean, we find three times more cooling from q_{upH} as from q_{upT} (Table 1). The spatial pattern of the cooling is very different: roughly globally uniform for q_{upT} (Fig.1c), and highly amplified at high latitudes for q_{upH} (Fig.1b). All these results are remarkably robust across models.

Another remarkable result is the linearity of the model responses: SST anomalies from combined CO_2 and OHU forcing are closely approximated by the sum of the responses to individual forcings, both globally and locally (see Table 1, and auxiliary material). We take the linearity as justification for studying the responses to CO_2 and OHU in isolation. While our primary interest is in the combined effects of CO_2 and OHU (our analog of transient global warming), the rest of this paper will simply compare the warming pattern from $2\times CO_2$ to the cooling patterns due to q_{upH} and q_{upT}.

3. Radiative feedback analysis

Our analysis is framed around a time- and zonal-mean TOA energy budget for perturbations to the control climate:

$$H(\phi) = \lambda(\phi)T(\phi) + R(\phi) - \nabla \cdot \mathbf{F}(\phi) \tag{3}$$

where H is the prescribed deep ocean heat sink ($H > 0$), R is the local radiative forcing, $\mathbf{F}$ is the anomalous northward atmospheric energy transport, and $\lambda(\phi)T(\phi)$ represents a linearization of the net radiative response about the local SST anomaly. $\lambda(\phi)$ is thus the local climate feedback (units of W m^{-2} K^{-1}), which can be decomposed into additive longwave (LW) and shortwave (SW) contributions from clear and cloudy sky. We can also define the global climate feedback in the usual way as $\lambda_G = (\overline{H} - \overline{R})/\overline{T}$, with the overbars denoting an area-weighted global mean. The global and local feedbacks are thus related by [e.g. *Armour et al.*, 2013]

$$\lambda_G = \overline{\lambda(\phi)T^*(\phi)}, \qquad T^*(\phi) \equiv \frac{T(\phi)}{\overline{T}} \tag{4}$$

In our OHU-only simulations $R = 0$, $H(\phi)$ is prescribed, and $\lambda(\phi)$ can be estimated directly from anomalous SST and TOA radiative fluxes at equilibrium. A different method must be used for $2\times CO_2$, as the TOA radiative fluxes include contributions from both feedback and forcing. We estimate $\lambda(\phi)$ and $R(\phi)$ for each model as the slope and intercept (respectively) of the local regression between TOA radiation and SST anomalies at each latitude under *transient* warming [*Crook et al.*, 2011]. To generate sufficient data for this analysis, we set the mixed-layer depth to 200 m, initialize each model with its control SST, and integrate for 40 years following abrupt CO_2 doubling. λ_G is then calculated from Eq.(4) using the equilibrium SST anomalies.

3.1. Global mean feedback

Multi-model estimates of λ_G are shown in Fig.1d-f (thick grey bars) for the three single-forcing scenarios ($2\times CO_2$, q_{upH}, q_{upT}). λ_G is very sensitive to the type of forcing. There is inter-model spread in the feedback estimate for each scenario, but the gross differences in overall feedback between the different forcing scenarios is robust. All models in our ensemble show that λ_G is 3 to 4 times more negative under q_{upT} than q_{upH}, consistent with the stronger global SST response to high-latitude OHU (Fig.1b-c). λ_G under $2\times CO_2$ is intermediate between these two extremes.

The decomposition in Fig.1d-f (thin colored bars) shows that the robustly less negative λ_G under q_{upH} relative to $2\times CO_2$ is largely due to cloud effects, with contributions from both LW (white bars) and SW (black bars). The strongly negative λ_G under q_{upT} is largely due to SW cloud effects, which are substantially more negative in every model in this scenario, while there is greater inter-model spread in the LW cloud response. In

all models the clear-sky LW component (red bars) is more negative under q_{upT} and less negative under q_{upH} relative to $2\times CO_2$.

Fig.1 establishes that the inter-model spread in λ_G and $T^*(\phi)$ for each forcing is substantially smaller than the model-mean differences between these forcing scenarios. We therefore suppose that model-independent insight into the reasons for the different sensitivities can be derived from a detailed analysis of a single model. In the following we examine the spatial structure of the response in CAM4, which features the most up-to-date physical parameterizations in our model ensemble. Key results and conclusions are qualitatively reproduced in the other models.

3.2. Local energy budget and feedback in CAM4

We wish to understand whether the differences in λ_G in response to different forcings can be explained in the context of fixed $\lambda(\phi)$ and different temperature patterns $T^*(\phi)$ [*Armour et al.*, 2013], or whether $\lambda(\phi)$ itself changes substantially under different forcings. We now analyze the TOA energy budget (Eq.(3)) for CAM4 under the three single-forcing scenarios in Fig.2a-c. For the OHU-only experiments, net radiation and heat transport divergence balance the imposed $H(\phi)$ at each latitude (black). For $2\times CO_2$, $\nabla\cdot\mathbf{F}$ balances net radiation (forcing plus feedback) everywhere.

From Fig.2b, q_{upH} is largely balanced by local radiation, dominated by the clear-sky LW component; high-latitude cloud changes have nearly compensating LW and SW effects. Heat transport is secondary in this case. Heat transport and local radiation are roughly equally important in balancing the forcing under q_{upT}. Tropical OHU efficiently cools

remote latitudes while high-latitude OHU does not. This is consistent with the strongly polar-amplified cooling under q_{upH} versus the globally uniform cooling under q_{upT}.

Fig.2d-f show the anomalous northward heat transport $\mathbf{F}$ decomposed into components due to moisture (latent heat) and dry static energy. The weakness of $\nabla \cdot \mathbf{F}$ under q_{upH} is associated with a near-cancellation of the dry and moist components of $\mathbf{F}$ across the mid-latitudes. Under q_{upT}, there are large changes in the partition of $\mathbf{F}$ across the tropics consistent with weakened poleward energy transport by the Hadley circulation, but $\mathbf{F}$ is dominated by latent heat in the extra-tropics. Under $2\times CO_2$ there are partially compensating changes in the dry and moist components but an overall increase in the poleward energy flux scaling with the moist component. This is consistent with the polar-amplified warming pattern [*Alexeev et al.*, 2005].

Fig.2g-i show estimates of the net local feedback $\lambda(\phi)$ in CAM4, along with its breakdown into LW and SW clear and (residual) cloud-sky components (the clear-sky SW component is positive but less than 0.2 W m^{-2} K^{-1} everywhere, not plotted). The different forcings excite very different local feedbacks; $\lambda(\phi)$ under both heat uptake scenarios differ substantially from the $2\times CO_2$ case (which we will denote $\lambda_{2\times}(\phi)$). Under q_{upH} the feedback is more positive (closer to zero) compared to $\lambda_{2\times}(\phi)$ everywhere equatorward of 50°, with the difference due primarily to a more positive SW cloud feedback. Under q_{upT} the shape of each feedback component is profoundly different, and the total $\lambda(\phi)$ is substantially more negative than $\lambda_{2\times}(\phi)$ everywhere except near the poles. A more negative clear sky LW component contributes to this pattern, but the largest difference is again found in the SW cloud component, which is strongly negative across the subtropics and

at the equator. Explanations for the very different sensitivities are thus to be found in the cloud regimes of the subtropics and within the ITCZ. SW cloud feedback is negative at high latitudes in all cases, attributable to an increase in optical thickness of cold clouds with temperature [*Zelinka and Hartmann*, 2012].

To summarize, our different forcing scenarios excite different feedback patterns, dominated by SW cloud effects. A mechanistic understanding of the dependence of feedback on forcing will focus on interactions between large-scale dynamics and cloud cover, and will be reported elsewhere.

3.3. Efficacy of ocean heat uptake

Our results show that the global cooling effect of OHU depends sensitively on its geographic structure. Moreover, we have identified a remarkable linearity in the responses to OHU and CO_2, such that their combined effect on global mean temperature is approximately additive: $\overline{T} = \overline{T}_{up} + \overline{T}_{2\times}$, where $\overline{T}_{up} = \overline{H}/\lambda_{Gup}$ and $\overline{T}_{2\times} = -\overline{R}_{2\times}/\lambda_{G2\times}$ are the global temperature responses to OHU and $2\times CO_2$, respectively. The global mean energy budget for transient global warming can thus be written

$$\varepsilon\overline{H} = \lambda_{G2\times}\overline{T} + \overline{R}_{2\times}, \qquad \varepsilon \equiv \lambda_{G2\times}/\lambda_{Gup} \tag{5}$$

where ε represents relative influence of OHU on global temperature compared to CO_2 forcing – the 'efficacy' of OHU as defined by Winton et al [2010]. Efficacy is thus readily interpreted as the ratio of global radiative feedbacks operating under CO_2 and OHU. Through Eq.(4) we can further write

$$\varepsilon^{-1} = 1 + \overline{\frac{\lambda_{2\times}(\phi)}{\lambda_{G2\times}}(T^*_{up}(\phi))'} + \overline{\frac{(\lambda_{up}(\phi))'}{\lambda_{G2\times}}T^*_{up}(\phi)} \tag{6}$$

where primes refer to deviations of OHU-only feedback and temperature responses from their values under $2\times CO_2$. Non-unit efficacy can thus result from different temperature patterns acting on fixed local feedbacks $\lambda_{2\times}(\phi)$ (the second term in Eq. (6), as discussed by *Armour et al.* [2013]), or by changes in the feedbacks themselves (third term in Eq. (6)).

ε is plotted in Fig.3 (blue bars); it is robustly greater than unity for q_{upH} (1.6 - 2.2) and smaller than unity for q_{upT} (0.5 - 0.6). The white bars show the component of efficacy due solely to changes in SST patterns (neglecting the third term in Eq.(6)). These are robustly close to unity in both scenarios. We conclude that *changes* in the local feedbacks set the non-unit efficacy of the different OHU patterns.

While we emphasize the robust aspects of our results, we also find some inter-model spread. Fig.3 shows that ε for q_{upH} differs between CAM3 and AM2 (1.56 versus 2.22). *Winton et al.* [2010] report consistent efficacy values for the corresponding coupled models CCSM3 and CM2.1 ($\varepsilon = 1.65$ and 1.99 respectively) over periods of transient warming wherein OHU occurs preferentially in the sub-polar oceans.

3.4. Temperature patterns in a diffusive model

Here we invoke a simple energy balance model to further understand the spatial structure of SST anomalies under different forcings. Following *Hwang and Frierson* [2010] we assume that $\mathbf{F}$ acts down the local gradient in near-surface moist static energy $m = c_pT + Lq$. We linearize for small perturbations as

$$\mathbf{F}(\phi) = -K\frac{d}{d\phi}\Big(T(1+f(\phi))\Big), \quad f(\phi) \equiv \frac{Lr}{c_p}\frac{dq^*}{dT}\Big|_{T_{ref}(\phi)} \tag{7}$$

where q^* is the saturation specific humidity, r is the relative humidity, and $T_{ref}(\phi)$ is the zonal-mean surface temperature from the control experiment. $f(\phi)$ depends only on the

mean state (assuming no change in r) and decreases strongly with temperature; the CAM4 control simulation gives $f = 4$ at the equator and 0.03 at the poles. We set $K = 1.5 \times 10^6$ W m^{-1} K^{-1} everywhere, consistent with *Hwang and Frierson* [2010].

Eqs. (7) and (3) define a boundary value problem ($\mathbf{F} = 0$ at the poles) for $T(\phi)$ given a forcing $R(\phi)$ and/or $H(\phi)$ and a feedback $\lambda(\phi)$. Fig.4 shows numerical solutions under our three single-forcing scenarios. We use the CAM4-derived $\lambda(\phi)$ for each scenario (Fig.2g-i) and $R(\phi)$ for $2\times CO_2$ as plotted in Fig.2a. We also plot solutions to the EBM using $\lambda = \lambda_{2\times}(\phi)$ for the heat uptake cases (dashed curves).

While this model is very crude (reducing atmospheric dynamics to a 1-D linear diffusion operator), it captures the different spatial patterns of warming and cooling, regardless of whether we use a OHU-specific feedback pattern or simply $\lambda_{2\times}(\phi)$. The nearly uniform cooling under q_{upT} results from efficient export of the moist static energy anomaly out of the tropics due essentially to the strong background moisture gradient between low and high latitudes. The strongly polar-amplified cooling under q_{upH} results from weak export of the moist static energy anomaly out of the high latitudes.

4. Discussion

OHU is an inherently transient phenomenon, but we have taken advantage of a separation of atmospheric and oceanic timescales to study the climatic significance of the spatial pattern of OHU in a quasi-equilibrium framework. We summarize our key results as follows: Tropical OHU produces a very modest cooling at all latitudes with weak efficacy relative to greenhouse gas forcing. High-latitude OHU produces three times more global cooling in a strongly polar-amplified pattern, and features a large efficacy relative

to greenhouse gas forcing. These results are robust across a small ensemble of GCMs (though all in consistent aquaplanet, perpetual equinox setups with no sea ice). We have rationalized the very different spatial patterns of the responses in terms of the asymmetrical response of the atmospheric moisture transport to high- versus low-latitude energetic perturbations, consistent with previous studies [*Alexeev et al.*, 2005; *Hwang and Frierson*, 2010]. Furthermore, our results cannot be understood in terms of a fixed local feedback and differing spatial patterns of temperature change as was found in the CCSM4 model by *Armour et al.* [2013]. We find instead first-order changes in $\lambda(\phi)$ under different forcing scenarios. We have shown that cloud SW effects are a key contributor to changes in $\lambda(\phi)$. This is qualitatively consistent with *Andrews et al.* [2012] who find substantial SW cloud feedback changes in transient coupled GCM simulations.

A few caveats deserve mention here. We have excluded surface ice and snow from the models, and thus eliminated a key positive feedback at high latitudes. We may therefore underestimate the (already very large) differences in responses to low- and high-latitude forcing. On the other hand, we may underestimate spatial variations in $\lambda(\phi)$, and the role of such variations in setting λ_G in the different scenarios. The perpetual equinox used in our calculations eliminates the seasonal cycle, pins the ITCZ permanently to the equator, and gives an overly strong equator-to-pole insolation gradient. It is not clear how all these inaccuracies (along with our idealized aquaplanet geometry) bias our results.

With these caveats in mind, we now briefly address some implications of our results. Transient climate sensitivity is governed both by an evolving pattern of sea-surface warming activating different local feedbacks, and by changes in the local feedbacks themselves

as the pattern of OHU slowly evolves. This points towards regional ocean circulations (setting different patterns of OHU) as a potentially important source of inter-model spread in transient climate projections. It also casts doubt on the possibility of estimating the feedbacks governing transient climate change from equilibrium mixed-layer models (as noted by *Shell* [2013]), and more importantly, of estimating equilibrium climate sensitivity from inherently transient climate observations.

More promisingly, the large robust changes in SW cloud feedback under our different forcing scenarios illustrate an important role for the ocean in setting one of the main radiative control knobs on the global climate system. A follow-up study will seek a mechanistic explanation for this link.

References

Alexeev, V., P. Langen, and J. Bates (2005), Polar amplification of surface warming on an aquaplanet in "ghost forcing"experiments without sea ice feedbacks, *Clim. Dyn.*, *24*, 655–666, doi:10.1007/s00382-005-0018-3.

Andrews, T., J. M. Gregory, M. J. Webb, and K. E. Taylor (2012), Forcing, feedbacks and climate sensitivity in CMIP5 coupled atmosphere-ocean climate models, *Geophys. Res. Lett.*, *39*, doi:10.1029/2012GL051607.

Armour, K. C., C. M. Bitz, and G. H. Roe (2013), Time-varying climate sensitivity from regional feedbacks, *J. Clim.*, *26*, 4518–4534.

Balmaseda, M. A., K. E. Trenberth, and E. Källén (2013), Distinctive climate signals in reanalysis of global ocean heat content, *Geophys. Res. Lett.*, *40*, doi:10.1002/grl.50382.

Bitz, C., K. Shell, P. Gent, D. Bailey, G. Danabasoglu, K. Armour, M. Holland, and J. Kiehl (2012), Climate sensitivity of the Community Climate System Model, version 4, *J. Clim.*, *25*, 3053–3070.

Blackburn, M., and B. J. Hoskins (2013), Context and aims of the aqua-planet experiment, *J. Meteor. Soc. Japan*, *91A*, doi:10.2151/jmsj.2013-A01.

Collins, W. D., et al. (2004), Description of the NCAR Community Atmosphere Model (CAM 3.0), *Tech. Rep. NCAR/TN-464+STR*, National Center for Atmospheric Research.

Crook, J. A., P. M. Forster, and N. Stuber (2011), Spatial patterns of modeled climate feedback and contributions to temperature response and polar amplification, *J. Clim.*, *24*, 3575–3592.

Delworth, T. L., et al. (2006), GFDL's CM2 global coupled climate models. Part i: Formulation and simulation characteristics, *J. Clim.*, *19*, 643–674.

Gregory, J. M. (2000), Vertical heat transports in the ocean and their effect on time-dependent climate change, *Clim. Dyn.*, *16*, 501–515.

Hansen, J., G. Russell, A. Lacis, I. Fung, D. Rind, and P. Stone (1985), Climate response times: Dependence on climate sensitivity and ocean mixing, *Science*, *229*, 857–859.

Hansen, J., et al. (2005), Efficacy of climate forcings, *J. Geophys. Res.*, *110*, doi:10.1029/2005JD005776.

Hwang, Y.-T., and D. M. W. Frierson (2010), Increasing atmospheric poleward energy transport with global warming, *Geophys. Res. Lett.*, *37*, doi:10.1029/2010GL045440.

Lee, M.-I., M. J. Suarez, I.-S. Kang, I. M. Held, and D. Kim (2008), A moist benchmark calculation for atmospheric general circulation models, *J. Clim.*, *21*, 4934–4954.

Lyman, J. M., S. A. Good, V. V. Gouretski, M. Ishii, G. C. Johnson, M. D. Palmer, D. M. Smith, and J. K. Willis (2010), Robust warming of the global upper ocean, *Nature*, *465*, doi:10.1038/nature09043.

Molteni, F. (2003), Atmospheric simulations using a GCM with simplified physical parameterizations. I: model climatology and variability in multi-decadal experiments, *Clim. Dyn.*, *20*, 175–191.

Neale, R. B., and B. J. Hoskins (2001), A standard test for AGCMs including their physical parameterizations: I: The proposal, *Atm. Sci. Lett.*, *1*, doi:10.1006/asle.2000.0019.

Neale, R. B., J. Richter, S. Park, P. H. Lauritzen, S. J. Vavrus, P. J. Rasch, and M. Zhang (2013), The mean climate of the Community Atmosphere Model (CAM4) in forced SST and fully coupled experiments, *J. Clim.*, *26*, 5150–5168.

Raper, S. C. B., J. M. Gregory, and R. J. Stouffer (2002), The role of climate sensitivity and ocean heat uptake on AOGCM transient temperature response, *J. Clim.*, *15*, 124–130.

Rose, B. E. J., and D. Ferreira (2013), Ocean heat transport and water vapor greenhouse in a warm equable climate: a new look at the low gradient paradox, *J. Clim.*, *26*, 2117–2136.

Shell, K. M. (2013), Consistent differences in climate feedbacks between atmosphere-ocean GCMs and atmospheric GCMs with slab-ocean models, *J. Clim.*, *26*, 4264–4281.

Table 1. The models used in this study, their horizontal and vertical resolution, and the global mean SST anomalies $\overline{T}$ obtained in each experiments (expressed relative to control runs, in K). Multi-model mean values are taken over the three full-physics models (CAM3, AM2.1, CAM4). All simulations use model default parameters except as noted in the text.

Model	Horizontal grid	Levels	$2\times CO_2$	q_{upH}	q_{upT}	$2\times CO_2+q_{upH}$	$2\times CO_2+q_{upT}$
CAM3	spectral T42	26	1.8	-1.6	-0.6	0.2	1.2
AM2.1	finite volume $2.0° \times 2.5°$	24	1.9	-2.1	-0.8	-0.2	1.3
CAM4	finite volume $1.9° \times 2.5°$	26	1.7	-1.5	-0.4	0.0	1.2
MITgcm	cubed-sphere C32	5	-	-1.2	-0.8	-	-
mean			1.8	-1.7	-0.6	0.0	1.2

Winton, M., K. Takahashi, and I. M. Held (2010), Importance of ocean heat uptake efficacy to transient climate change, *J. Clim.*, *23*, 2333–2344.

Yu, L., and R. A. Weller (2007), Objectively analyzed air-sea heat fluxes for the global ice-free oceans (1981–2005), *Bull. Amer. Meteor. Soc.*, *88*, 527–539.

Zelinka, M. D., and D. L. Hartmann (2012), Climate feedbacks and their implications for poleward energy flux changes in a warming climate, *J. Clim.*, *25*, 608–624.

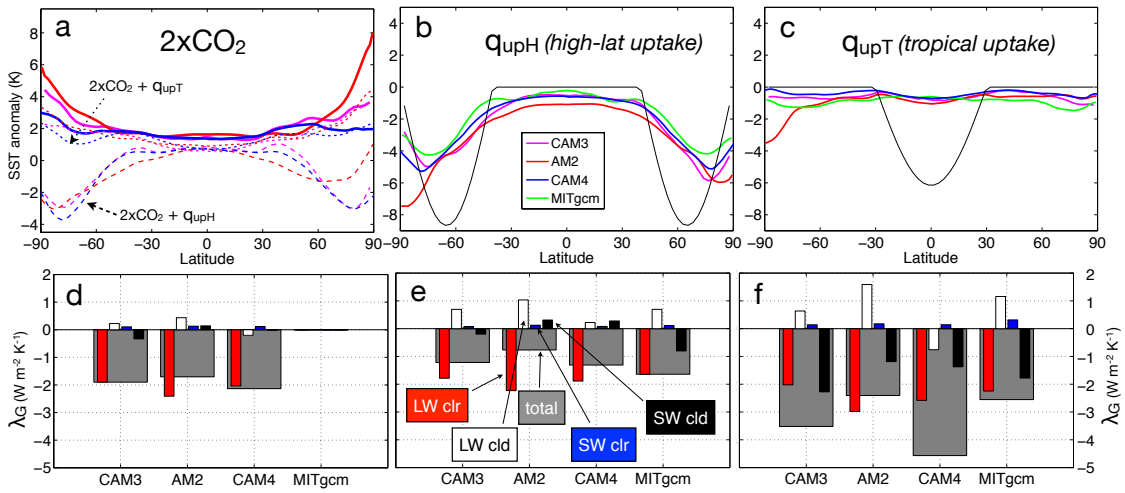

Figure 1. Multi-model study of climate sensitivity to prescribed ocean heat sinks compared to greenhouse gas forcing. Panels (a)-(c): equilibrium SST anomalies relative to control simulations for each model. Panel (a) shows the response to $2\times CO_2$ alone (solid) and the responses to combined $2\times CO_2$ plus prescribed OHU in the high latitudes (q_{upH}, Eq.(1), dashed) and tropics (q_{upT}, Eq.(2), dotted). Panels (b) and (c) show responses to OHU alone, with the prescribed heat sinks also plotted in W m^{-2} (thin grey). Panels (d)-(f): estimates of global mean feedback λ_G under the three single-forcing scenarios. For each model and each forcing, the total feedback is shown in thick grey bars, along with its decomposition into LW and SW clear and cloudy-sky components.

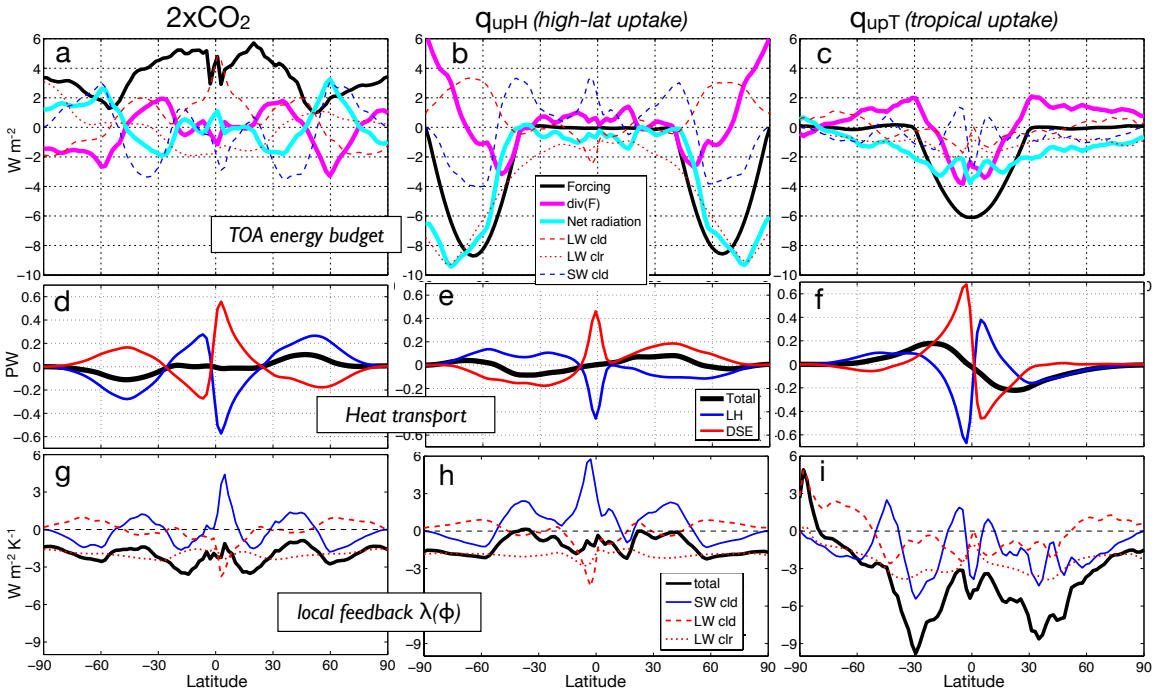

Figure 2. Spatial structure of the energy budget for CAM4 under the three forcing scenarios. (a)-(c): the forcing (black) plotted with anomalous heat transport divergence (magenta), net TOA radiation (cyan), and its breakdown into SW and LW components (the clear-sky SW component is near zero and not shown). For $2\times CO_2$ the forcing is estimated from the intercept of the regression line from the transient adjustment of the deep slab. (d)-(f): anomalous northward energy flux, decomposed into latent heat and dry static energy components. (g)-(i): local feedback $\lambda(\phi)$ for CAM4. For $2\times CO_2$ the feedbacks are calculated from the transient adjustment of a 200 m mixed-layer model. For the pure heat uptake cases the feedbacks are estimated from the equilibrium TOA radiative anomalies normalized by the local surface ΔT. In all cases the SW clear-sky component is very small and not shown.

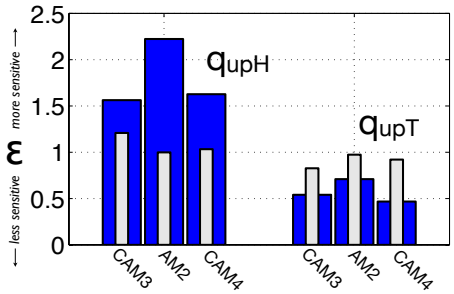

Figure 3. Efficacy of OHU relative to $2\times CO_2$ in our two scenarios. Blue bars show actual efficacy; white bars show the component due to differences in surface temperature patterns, neglecting the third term in Eq.(6). The difference between white and blue bars can be attributed to the differences in feedback $\lambda(\phi)$ in different scenarios.

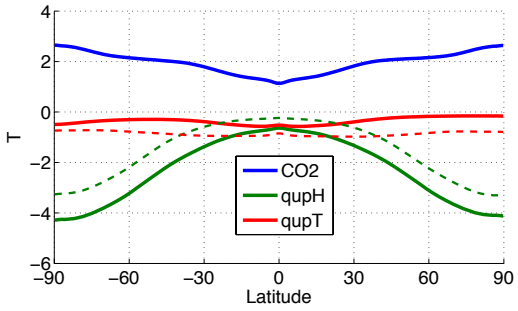

Figure 4. Zonal-mean temperature anomalies from the diffusive EBM. Solid curves use CAM4-derived forcing and feedback diagnosed from each experiment (Fig.2). Dashed curves use $\lambda = \lambda_{2\times}(\phi)$ for all cases.

Auxiliary Material for

The dependence of transient climate sensitivity and radiative feedbacks on the spatial pattern of ocean heat uptake

Brian E. J. Rose

(University at Albany, Albany, New York)

Kyle C. Armour

(Massachusetts Institute of Technology, Cambridge, Massachusetts)

David S. Battisti

(University of Washington, Seattle, Washington)

Nicole Feldl

(California Institute of Technology, Pasadena, California)

Daniel D. B. Koll

(University of Chicago, Chicago, Illinois)

Geophysical Research Letters, 2013

Introduction

This auxiliary material contains two sections, each with one figure (Figs. A1 and A2): 1. A comparison between ocean heat uptake (OHU) patterns employed in the manuscript to those found within fully-coupled general circulation models; 2. An analysis of the linearity of model responses to OHU and CO_2 forcing.

1. Heat uptake in CMIP5 models

Fig.A1 shows the anomalous surface heat flux following an abrupt quadrupling of CO_2, from an ensemble of general circulation models (GCMs) participating in the Coupled Model Intercomparison Project phase 5 (CMIP5) [Taylor et al., 2012]. While the surface flux anomaly pattern is variable across models, some common features can be seen: substantial OHU occurs at all latitudes immediately following the abrupt onset of forcing (Fig.A1a); after several decades, however, heat is taken up almost exclusively in the subpolar oceans (Fig.A1b). Our idealized OHU curves are overlain for reference. Together, q_{upH} and q_{upT} broadly capture the patterns of OHU as simulated by the CMIP5 models: OHU uptake several years after CO_2 quadrupling

involves a combination of q_{upH} and q_{upT}, while OHU after several decades most closely resembles q_{upH}.

2. Linearity of model responses

Here we briefly document the linearity of the responses of our three comprehensive GCMs to combined CO_2 and OHU forcing. Fig.A2 shows anomalous SST (upper panels) and net top-of-atmosphere (TOA) radiation (lower panels) for $2xCO_2$ in the presence of high-latitude OHU (solid blue) and low-latitude OHU (solid red). The dashed lines show the sum of the responses to $2xCO_2$ and OHU alone. Departures of the linear estimates (dashed) from the combined forcing results (solid) can indicate non-linearity in the model responses or simply insufficient integration time to average over the modeled natural variability. We find that the linear estimates are very close to the actual combined forcing results. The largest departures are found near the poles, which is consistent with the expectation of large natural variability of polar climates. Of the three GCMs, AM2 appears to be the least additive, particularly in the TOA radiation. It is not clear whether this is indicative of actual non-linearity or not; a longer integration of this model would help rule out the role of natural variability.

References

Taylor, K. E., R. J. Stouffer, and G. A. Meehl (2012), An overview of CMIP5 and the experiment design, Bull. Amer. Meteor. Soc., 27, pp. 485–498, doi:10.1175/BAMS-D-11-00094.1.

Figure Captions

Figure A1: Net surface heat flux anomalies (positive up) in CMIP5 models immediately following abrupt quadrupling of CO_2 (a) and after 100 years (b). Black curve shows ensemble mean of 16 different coupled models. Also shown: the idealized heat uptake curves used in our aquaplanet simulations: q_{upH} (blue) and q_{upT} (red). The CMIP5 models used here are ACCESS1-0, bcc-csm1-1, CanESM2, CCSM4, CSIRO-Mk3-6-0, GFDL-CM3, GFDL-ESM2G, GFDL-ESM2M, inmcm4, IPSL-CM5A-LR, IPSL-CM5B-LR, MIROC5, MIROC-ESM, MPI-ESM-LR, MRI-CGCM3, and NorESM1-M.

Figure A2: Linearity of the models to combined CO_2 and OHU forcing. We plot SST anomalies in the upper panels (a-c) and net TOA radiation anomalies in the lower panels (d-f). Solid curves are from the combined forcing simulations; dashed curves are the sum of the responses from the single-forcing simulations.

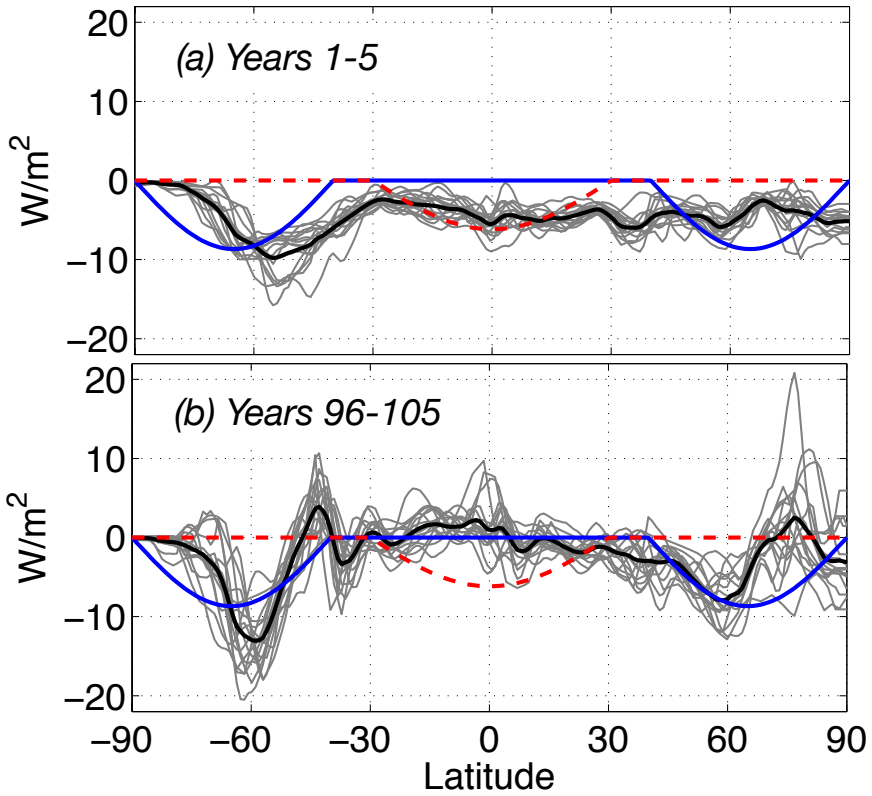

Figure A1: Net surface heat flux anomalies (positive up) in CMIP5 models immediately following abrupt quadrupling of CO_2 (a) and after 100 years (b). Black curve shows ensemble mean of 16 different coupled models. Also shown: the idealized heat uptake curves used in our aquaplanet simulations: q_{upH} (blue) and q_{upT} (red). The CMIP5 models used here are ACCESS1-0, bcc-csm1-1, CanESM2, CCSM4, CSIRO-Mk3-6-0, GFDL-CM3, GFDL-ESM2G, GFDL-ESM2M, inmcm4, IPSL-CM5A-LR, IPSL-CM5B-LR, MIROC5, MIROC-ESM, MPI-ESM-LR, MRI-CGCM3, and NorESM1-M.

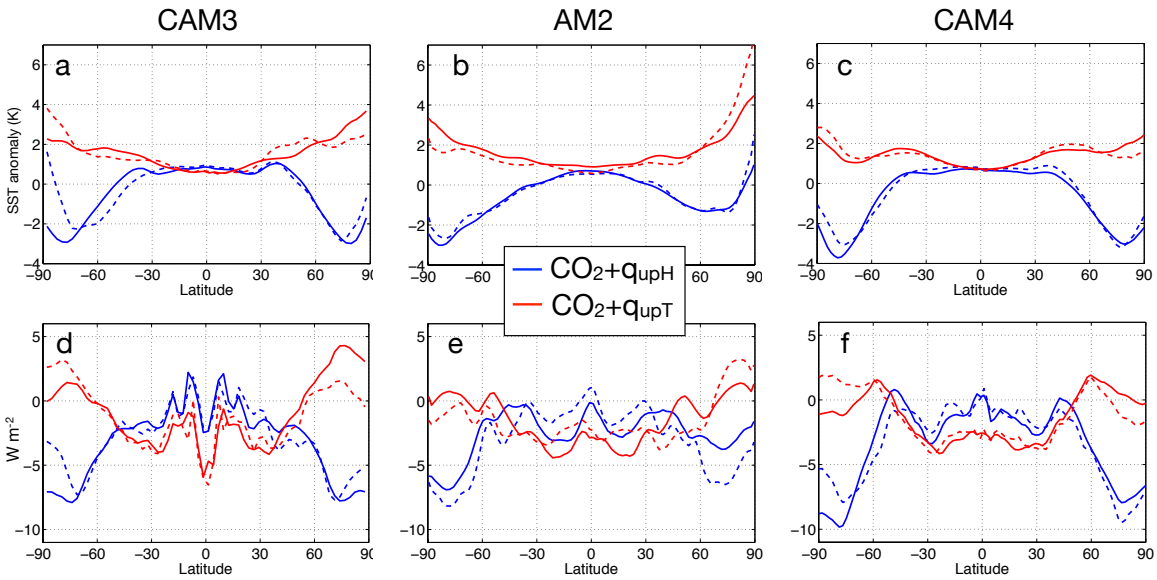

Figure A2: Linearity of the models to combined CO_2 and OHU forcing. We plot SST anomalies in the upper panels (a-c) and net TOA radiation anomalies in the lower panels (d-f). Solid curves are from the combined forcing simulations; dashed curves are the sum of the responses from the single-forcing simulations.